

小电流脉冲 TIG 弧的谐振现象及其交流阻抗特性分析

牛 永¹, 宋永伦², 曾周末¹

(1. 天津大学 精密测试技术及仪器国家重点实验室, 天津 300072

2. 北京工业大学 机械工程与应用电子技术学院, 北京 100124)

摘 要: 采用直流叠加高频正弦的方法对小电流 TIG 弧的交流阻抗特性进行了研究, 发现随频率的增大, 电弧阻抗的模量先增大后又减小; 而其复角随频率的增大持续减小, 在模量的最大值减小为零, 很显然, 电弧阻抗存在谐振点. 经过对不同频率的激励电流和响应电压进行数据分析, 得到了小电流 TIG 弧的高频动态阻抗电路模型以及传递函数. 应用数学分析软件拟合出小电流 TIG 弧的阻抗曲线, 确定了在测试条件下模型中的参数, 并计算出电弧的谐振频率.

关键词: 脉冲电弧; 电弧模型; 谐振; 动态阻抗

中图分类号: TG403 文献标识码: A 文章编号: 0253-360X(2011)02-0013-04



牛 永

0 序 言

脉冲 TIG 弧对于直流 TIG 弧在物理特性方面有着显著的不同. 平均电流相同时电磁收缩效应增大, 轴向的指向性增强; 电弧压力增大, 熔透性增加, 同时熔池受到超声波振动, 有利于改善焊缝物理化学冶金过程并增加了熔池流动性. 对焊接较薄的金属材料, 这些特点有利于焊缝质量的提高, 特别适于快速焊接^[1].

当前对脉冲 TIG 弧的电特性和传递函数有了一些研究, 一般都认为电弧具有热惯性, 从热惯性的角度开始进行分析, 并基于 Mayr 电弧方程, 即

$$\frac{dQ}{dt} = EI - P_0 \quad (1)$$

得出电弧的传递函数^[2-8].

$$G_h(s) = \frac{R_m - Qs + R_{vf}}{Qs + 1}$$

Mayr 方程认为, 电弧的能量输入减去耗散等于热量的变化. 这种假设的前提为: 电弧是阻性体. 然而电弧组成决定了其本身并不只存在阻性. 由此方程 (1) 及此传函不适用于高频电弧.

与 Mayr 方程从热力学平衡的研究角度不同, 文中从电弧电特征的表现来研究小电流 TIG 弧, 用不

同频率的正弦电流冲击直流 TIG 弧, 由此来分析电弧的电流电压对频率的响应情况, 从而归纳出小电流 TIG 弧的高频动态阻抗特性, 提出了电弧的一种高频电特性模型, 并推导出其传递函数.

1 试验方法

测试结构如图 1 所示. 恒流源的输出电流 1 ~ 10 A 可调, 内置大电感, 电流输出稳定. 交流源采用信号发生器并配有功率放大, 输出频率可达兆赫以上. 隔直电容采用高耐压、高容量、低漏电、无极性的 CBB 电容, 以实现较大功率的电流传输. 采样电阻输出的电压表征电弧的电流信号, 采用无感功率电阻, 以减小测试系统的误差.

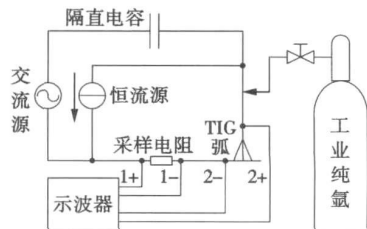


图 1 测试解构示意图

Fig 1 Schematic diagram of measurement structure

DSO6014A既可以快速地观察波形,又可以把波形画面和数据保存起来并传送给计算机,便于试验调试和数据分析.示波器探头1通过测试采样电阻两端的电压,得到电弧的电流;探头2直接测试电弧的电压.测试过程中,由于工件接正,所以探头2测得的电压为负值,在示波器上选择信号极性反转功能,使其值为正,以便于观测和分析.保护气采用工业纯氩,流量调节至 5 L/min ;试验过程中,氩气流量不变.

在测试过程中,首先把恒流源输出电流调至测试值,然后再调整交流电源,使其输出一定幅值的交流正弦,利用示波器记下电流电压的波形和数据.然后改变交流源的输出频率,分别测试,得到在不同频率下电弧的电流电压曲线和数据.

2 电弧阻抗测试

在测试过程中,基值电流设定至 3 A 叠加正弦的峰峰值调整为 1 A 频率调节范围 $1\text{ kHz}\sim 2\text{ MHz}$ 得到一系列电弧的电流电压波形.图2为其中四个频率下的电流电压波形,图2 a~d的频率分别为 1 kHz 、 10 kHz 和 1 MHz .

从图2中可以看出电弧电压交流成分的相位和幅值的变化.在相位方面, 1 kHz 时,电压相位超前电流相位;在 10 kHz 时,电压超前的相位变小;频率增至 100 kHz 电压相位反而滞后于电流相位;到 1 MHz 时,滞后相位变得更大.从幅值上看,电弧电压交流成分的幅值随频率的上升先变大,随后慢慢变小.

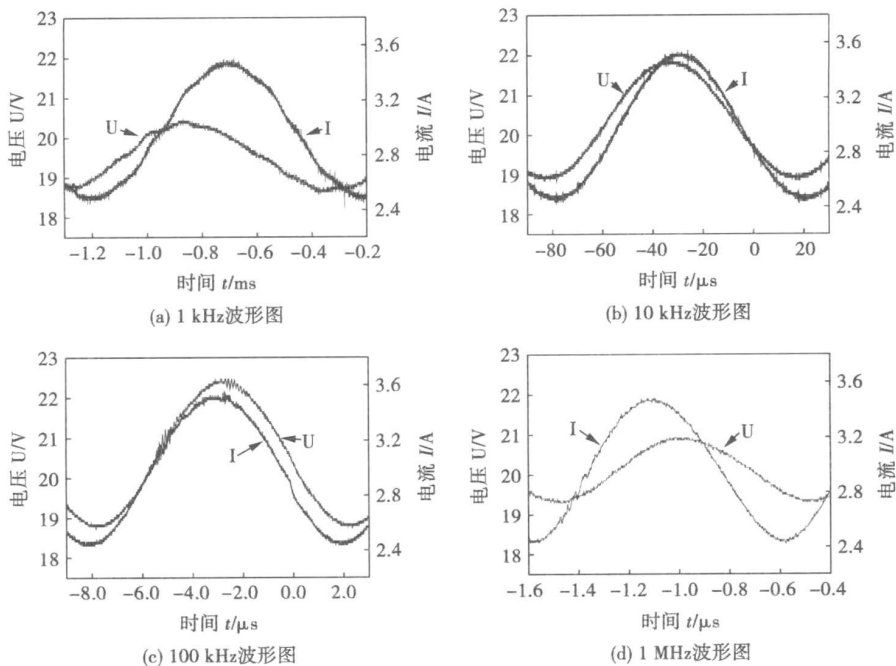


图 2 电弧电流电压波形

Fig 2 Current and voltage waves of arc

很显然,电弧的动态阻抗传递函数并非一阶惯性环节,而明显的带有二阶震荡特征,同时电弧存在谐振点,从图2粗略来看,在测试条件下,TIG弧的谐振频率在 $10\sim 100\text{ kHz}$ 之间.

3 数据分析

3.1 电压与电流交流成分的相位差与幅值比

为测定小电流 TIG弧的动态电特性,需从不同频率的电流电压波形中提取出交流分量进行相位与

幅值的比较.测试得到的电压电流信号,存在许多杂波干扰,而且测试时设定的激励频率与实际输出信号的频率也有一定的误差,为了消除这些干扰和误差,这里采用频域分析的方法,把测试的数据进行离散傅立叶变换,从而可以得到真实的激励频率以及输入和输出在此频率下的幅值和相位.数据变换过程如下式所示,即

$$X(k) = \sum_{j=1}^N x(j) \omega_N^{(j-1)(k-1)}$$

式中: ω_N 为 $e^{-2\pi j/N}$; $x(j)$ 为输入测试点; $X(k)$ 为得

到的变换值。

对每一频率下的电压、电流两部分数据进行变换, 在输入的激励频率附近, 从得到的变换值 $X(k)$ 中, 找到其模量的极大值 A_2, A_1 和此极大值对应的频率, f 以及在此频率下对应的幅角 θ 。由此得到电压电流幅值比和相位差, 即动态阻抗的幅值与相角。

$$K = A_2 / A_1 \quad (2)$$

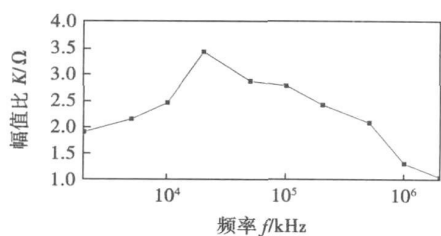
$$\Delta\theta = \theta_U - \theta_I \quad (3)$$

不同频率下的电流、电压的相位、幅值以及幅值比、相位差, 如表 1 所示。把表中 $K, \Delta\theta$ 对于频率 f 绘制出曲线, 如图 3 所示。

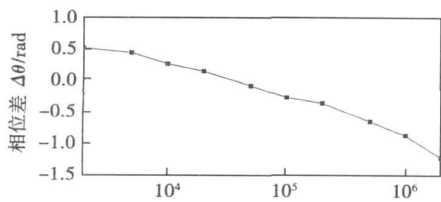
表 1 电弧电压、电流交流成分的幅值、相位

Table 1 Amplitude and Phase of alternating component of voltage and current of arc

激励频率 f/kHz	电压幅值 A_U/V	电流幅值 A_I/A	幅值比 K/Ω	电压复角 θ_U/rad	电流复角 θ_I/rad	复角差 $\Delta\theta/\text{rad}$
1.011	0.704 0	0.468 0	1.504	2.962	2.284	0.678 0
2.035	0.888 3	0.468 6	1.896	2.817	2.305	0.512 0
5.054	1.050	0.490 0	2.143	-0.530 6	-0.972 2	0.441 6
10.11	1.321	0.538 0	2.455	-2.470	-2.734	0.264
20.22	1.695	0.495 8	3.419	-1.903	-2.050	0.147
50.23	1.366	0.477 8	2.859	0.052 49	0.140 2	-0.087 71
100.5	1.374	0.494 9	2.776	0.138 8	0.412 5	-0.273 7
203.5	1.340	0.555 4	2.413	-2.461	-2.096	-0.365
506.6	1.108	0.535 0	2.071	-1.837	-1.183	-0.654
1001	0.758 6	0.583 6	1.300	0.795 8	1.672	-0.876
2014	0.450 8	0.434 0	1.039	-1.926	-0.701 8	-1.224



(a) 频率-幅值比



(b) 频率-相位差

图 3 电弧电压、电流交流成分的幅值比与相位差

Fig. 3 Amplitude ratio and Phase difference of alternating component of voltage and current of arc

从图 3 可以看出, 在激励电流频率从小到大的变化过程中, 电弧动态阻抗的幅值由小变大, 在 20 ~ 50 kHz 之间, 达到最大值, 然后随着频率的增加, 动态阻抗的幅值变得越来越小。同样的, 动态阻抗的相角也在 20 ~ 50 kHz 附近达到零点。由此看出, 在此测试条件下, 电弧动态阻抗存在谐振点, 并且谐振点在 20 ~ 50 kHz 之间。

3.2 电弧的交流阻抗模型

由上面的数据特征可推测电弧的交流阻抗模型如图 4 所示。

电路中的电容 C 和电感 L 决定电弧的谐振点, 在低频情况下, 二者并联的阻抗表现为感性, 电流滞后于电压; 在高频情况下, 二者并联的阻抗表现为容性, 电流超前于电压, 这与图 2 图 3 的测试结果一致。电阻 R 调整交流阻抗使电弧在谐振点的电阻不会无穷大, 而要趋近谐振点的交流分量的电阻。

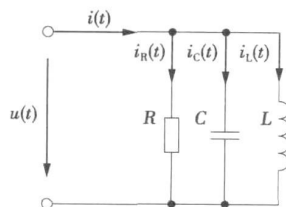


图 4 电弧交流阻抗模型

Fig. 4 Alternating current impedance model of arc

根据基尔霍夫电流定律 (KCL) 有

$$\dot{i}(t) + \dot{i}_R(t) + \dot{i}_C(t) + \dot{i}_L(t) = \dot{i}(t) \quad (4)$$

将 $\dot{i}_R(t) = \frac{u_C(t)}{R}$, $\dot{i}_C(t) = C \frac{du_C(t)}{dt}$, $u_C(t) = L \frac{di_L(t)}{dt}$

代入 (4), 整理得

$$C \frac{d^2 u_C(t)}{dt^2} + \frac{1}{R} \frac{du_C(t)}{dt} + \frac{1}{L} u_C(t) = \frac{d\dot{i}(t)}{dt} \quad (5)$$

对式 (5) 进行拉氏变换, 得到电弧交流阻抗的传递函数为

$$Z(s) = \frac{U(s)}{I(s)} = \frac{s}{Cs^2 + \frac{1}{R}s + \frac{1}{L}} \quad (6)$$

令 $s = \sigma + j\omega$ 中的 $\sigma = 0$ 即 $s = j\omega$

$$Z(j\omega) = \frac{j\omega}{C(j\omega)^2 + \frac{1}{R}(j\omega) + \frac{1}{L}}$$

$$= \frac{1}{\frac{1}{R} + \left(\frac{1}{G\omega} - \frac{1}{L\omega} \right) j}$$

$Z(\omega)$ 的模为

$$|Z(\omega)| = \frac{1}{\sqrt{\frac{1}{R^2} + \left(C\omega - \frac{1}{L\omega}\right)^2}} \quad (7)$$

和复角

$$\phi(\omega) = \arctan\left[R\left(\frac{1}{L\omega} - C\omega\right)\right] \quad (8)$$

分别表示该输入阻抗的模量和相角随频率的变化关系。共振角频率 $\omega_0 = 1/\sqrt{LC}$

3.3 参数拟合

利用 matlab 的 cftool 工具箱对试验数据按式 (7)、式 (8) 进行拟合。

对于式 (7) 拟合等式为

$$f(x) = 1 / (1 / (R * x) + (1 / (L * x) - C * x)^2)$$

0.5

最后得到 CIR 的值为

$$C = 9.81 \times 10^{-8} \quad L = 0.0002226 \quad R = 2.76$$

同样的方法对式 (8) 拟合, 拟合等式为

$$f(x) = \text{atan}\left(\frac{1}{L * x} - C * x\right) * R$$

可得 CIR 值

$$C = 9.895 \times 10^{-8} \quad L = 0.0003341 \quad R = 2.336$$

两者拟合得到的结果有一些差距, 一般来说, 幅值的大小受到测量设备和测量环境影响较大, 而相位测量时受影响较小。按 0.4 和 0.6 的权重分配得到最终的参数值

$$C = 9.861 \times 10^{-8} \quad L = 0.0002895 \quad R = 2.506$$

由以上的最终参数做得的波特图如图 5 所示。

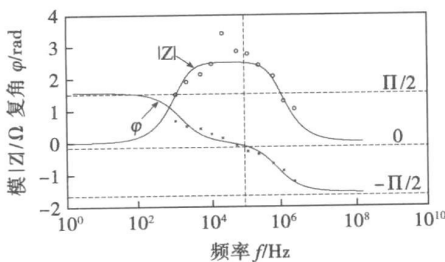


图 5 TIG 弧动态阻抗的波特图

Fig 5 Bode diagram of dynamic impedance of TIG arc

由此得出在此测试条件下的共振频率为:

$$f = \frac{\omega_0}{2\pi} = \frac{1}{2\pi \sqrt{LC}} = 29.88 \text{ kHz}$$

4 结 论

(1) 脉冲小电流 TIG 弧的高频阻抗并非一阶特性而是具有二阶共振特性。

(2) 根据 CIR 并联电路的电学特征, 使电弧工作在谐振点, 得到最大的电弧输入功率, 从而提高焊接效率。

参考文献:

- [1] 姜焕中. 电弧焊及电渣焊[M]. 2版. 北京: 机械工业出版社, 1995.
- [2] 张立斌. 弧焊质量自动控制基础[M]. 哈尔滨: 哈尔滨工程大学出版社, 2007.
- [3] 卢本. 焊接电弧的数学模型[J]. 电焊机, 1983(5): 18-20. Lu Ben. The mathematical model of arc welding[J]. Electric Welding Machine, 1983(5): 18-20.
- [4] 赵家瑞, 张东元, 孙栋, 等. 矩形波直流脉冲 TIG 焊电弧稳定性的研究[J]. 焊接学报, 1988, 9(3): 171-180. Zhao Jiarui, Zhang Dongyuan, Sun Dong et al. Study of arc stability in high frequency pulsed TIG welding with rectangular waves[J]. Transactions of the China Welding Institution, 1988, 9(3): 171-180.
- [5] 赵家瑞, 李义丹. 高频脉冲 TIG 焊的电弧控制及高频效应[J]. 天津大学学报, 1989, 3: 25-32. Zhao Jiarui, Li Yidan. Control over arc of pulsed high frequency TIG welding and high frequency effect[J]. Journal of Tianjin University, 1989, 3: 25-32.
- [6] Yang Lijun, Han Pengbo, Dong Tianshu et al. Simulation on dynamic characteristic of negative resistance arc in pulsed TIG welding[J]. Transactions of Tianjin University, 2007, 13(1): 62-66.
- [7] 董天顺, 杨立军, 梁建军. 小电流脉冲 TIG 焊电弧动态特性的 Matlab 仿真[J]. 焊接技术, 2003, 32(3): 11-13. Dong Tianshu, Yang Lijun, Liang Jianjun. Simulation study on arc dynamic characteristic in low current pulsed TIG welding with Matlab\Simulation[J]. 2003, 32(3): 11-13.

作者简介: 牛永, 男, 1974 年出生, 博士研究生, 主要从事电弧诊断与信号分析方面的研究, 发表论文 9 篇, Email: n1988@scfu.com

MAIN TOPICS, ABSTRACTS & KEY WORDS

Aging embrittlement of Super 304H steel welded joint LI Ximei, ZOU Yong, ZOU Zengda, ZHANG Zhongwen (1. Key Laboratory of Liquid Structure and Heredity of Materials, Ministry of Education, Shandong University, Jinan 250061, China; 2. Shandong Electric Power Research Institute, Jinan 250002, China), P 1—4, 24

Abstract The embrittlement of welded joints of Super 304H steel was investigated by means of scanning electron microscopy, energy dispersive spectroscopy, transmission electron microscopy, X-ray diffraction analysis and the impact test. The experimental results indicate that the microstructure of welded joints consists of matrix and precipitated phase. The reason of embrittlement of welded joint is that $Cr_{23}C_6$ precipitated along coarse grain boundary and the amount of precipitation are the key factors. After being aged at 650 °C, there are obvious precipitated Nb(C, N) and $Cr_{23}C_6$ phases in welded joint and the amount of precipitate reaches a stable value with the increasing of aging time. The precipitation of $Cr_{23}C_6$ causes the intergranular embrittlement of welded seam, the impact energy of welded joint reduces rapidly and the fracture mode turns to intergranular fracture. The toughness of welded joint of Super 304H steel depends on the microstructure of the matrix under welded condition.

Key words aging treatment, austenitic steel, welded joint, embrittlement

Effect of laser remelting on erosion behavior of plasma sprayed thermal barrier coatings WANG Dongsheng², TIAN Zongjun², WANG Jingwen¹, SHEN Lidai², HUANG Yinhu² (1. Department of Mechanical Engineering, Tongling College, Tongling 244000, China; 2. College of Mechanical and Electrical Engineering, Nanjing University of Aeronautics and Astronautics, Nanjing 210016, China), P 5—8

Abstract The $ZrO_2-7\% Y_2O_3$ thermal barrier coatings fabricated by plasma spraying on TiAl alloy surface were remelted by laser. The microstructures of the plasma sprayed and laser remelted coatings were compared by using scanning electron microscopy (SEM). Meanwhile, the erosion experiments of the coatings were carried out and the erosion failure mechanisms were discussed. The results show that the as-sprayed ceramic coating has a typical lamellar stacking characteristic. However, the laser remelted coating exhibits a compact remelted zone which is composed of column-like grains along the direction of the heat current. The laser remelted coating has better erosion resistance than the plasma sprayed coating. Both as-sprayed and laser remelted coatings show a brittleness erosion mechanism. Owing to the limited bonding at the interfaces between lamellar the spalling of ceramic particles from the lamellar interface may

be mainly responsible for the erosion of the as-sprayed coating. In contrast, cracking occurs within region near the surface of the laser remelted ceramic coating which makes erosion occur by removal of these small blocks.

Key words laser remelting, plasma spraying, thermal barrier coatings, erosion resistance, failure mechanism

Development and application of ultrasonic TOFD testing system with USB SHENG Zhaoyang, GANG Tie, CHI Dazhao, HUANG Jiangzhong, LI Yinan, ZHAO Weijun (1. State Laboratory of Advanced Welding Production Technology, Harbin Institute of Technology, Harbin 150001, China; 2. Harbin Boiler Company Limited, Harbin 150046, China), P 9—12

Abstract A testing system based on expanded ultrasonic TOFD (time of flight diffraction) with USB was presented for thick-walled weld inspection. And the cross-correlation algorithm was used to correct the distorted testing image for defect identification. The system was applied on the boiler weld testing at the workshop. The results show that the D scan image is clear and the defects can be recognized quickly. The distortion of testing image was well avoided by cross-correlation algorithm. The developed system is open, which can be updated according to the requirement. The testing processing can be easily implemented. So the system is suitable for weld detection and could provide referenced data for the quality evaluation of weld.

Key words ultrasonic diffraction, weld testing, signal collection, pressure vessel testing, image correction

Resonance phenomenon of small current pulsed TIG arc and analysis of AC impedance features NIU Yong, SONG Yongjun, ZENG Zhoudo (1. State Key Laboratory of Precision Measurement Technology and Instruments, Tianjin University, Tianjin 300072, China; 2. College of Mechanical Engineering & Applied Electronics Technology, Beijing University of Technology, Beijing 100124, China), P 13—16

Abstract A method that alternating sine current superposes on direct current was adopted for study on alternating current impedance of the small current TIG arc. It was found that with the frequency getting high, the modulus of arc impedance increased and then decreased, and the phase angle decreased continuously. The maximum of the modulus just coincided with the zero point of phase angle, and obviously arc impedance had a resonance. By analyzing the voltage and current data in many different frequencies, the electronic model and transfer function of TIG arc alternative component were deduced. The parameters of transfer function were fit by using mathematics software, and the resonance frequency was calculated.

Key words pulsed arc, arc modulus, resonance, dy-

nanic impedance

Friction stir welding process parameter optimization of 7A52 aluminum alloy LIANG Zhifang¹, SHI Qingyu, KANG Xu¹ (1. Department of Mechanical Engineering, Tsinghua University, Beijing 100084, China; 2. Department of Mechanical & Electrical Engineering, North China Institute of Science & Technology, Beijing 101601, China), P 17—20

Abstract The joint strength of friction stir welding is an important indicator of performance. Through different combinations of welding parameters such as tool rotation rate, tool traverse speed and target depth, 35 friction stir welded test plates of 7A52 aluminum alloy are prepared. The tensile strength of welded joints of the test plates is detected by tensile test. The regression model between the tensile strength of welded joints and welding process parameters is established. When the tool rotation rate n , the tool traverse speed v or the target depth d individually changes, there is a peak of joint tensile strength. The tool rotation rate and the tool traverse speed interactively impact the tensile strength by means of n/v . It is proved that the optimized welding parameters can make joint tensile strength be up to 384.06 MPa.

Key words friction stir welding; tensile strength; welding process parameter

Numerical simulation on 201 stainless steel spot welding process SUN Fangfang, LI Mengsheng, WANG Yang, ZHAO Ying (School of Materials Science and Engineering, Hefei University of Technology, Hefei 230009, China), P 21—24

Abstract Temperature and residual stress field of 201 stainless steel spot welding process were simulated by Ansys finite element software. The characteristics of spot heating and cooling and the temperature distribution were analyzed, and the diversification and distribution of stress were discussed. The results show that with spot welding heating, symmetrical ellipse nugget gradually forms along the joint surface, and compressive stress is mainly in the nugget. At cooling moment, the isotherm of welding area reduces with the shape of ellipse, and the stress in nugget transforms to tensile stress. The actual nugget sizes of spot welding joints are measured to verify that the simulation results are accurate and reliable.

Key words numerical simulation; 201 stainless steel; temperature field; stress field

Mode for near surface defect detection based on ultrasonic TOFD CHIDA Zhao¹, GANG Tie, YAO Yingxue, YUAN Yuan, SHENG Chaoyang (1. State Key Laboratory of Advanced Welding Production Technology, Harbin Institute of Technology, Harbin 150001, China; 2. School of Mechatronics Engineering, Harbin Institute of Technology, Harbin 150001, China), P 25—28

Abstract Aims at the problem of near surface dead zone in ultrasonic TOFD (time of flight diffraction) method, a modi-

fied testing mode named as TOFDW, which employs the three-fold reflected longitudinal wave from the bottom of the piece under testing, is presented based on the conventional TOFD technique. The characteristic of sound propagation in TOFDW mode is analyzed and its detection principle is illustrated. Through artificial defect testing, the features of tested signal and image are cognized, and the testing sensitivity and accuracy of the testing mode are studied. Weld piece is tested and the result is verified by destructive testing. The experimental results show that TOFDW model can identify the near surface defect that cannot be distinguished by using conventional methods, and the artificial defect with buried depth of 1.0 mm can be effectively detected. The model has a high quantitative accuracy, and the average absolute error of artificial defects location is less than 0.3 mm.

Key words ultrasonic TOFD; near surface dead zone; defect detection

Real-time visual detection of welding pool in double electrode MIG welding SHI Yu, WANG Haitao, XUE Cheng, LIU Xiaotian¹ (1. State Key Laboratory of Gansu Advanced Non-Ferrous Metal Materials, Lanzhou University of Technology, Lanzhou 730050, China; 2. Key Laboratory of Non-Ferrous Metal Alloys and Processing of Ministry of Education, Lanzhou University of Technology, Lanzhou 730050, China), P 29—32

Abstract An efficient bypass arc welding method was presented by employing common CCD camera with composite filter glass. The clear image of welding pool was captured under the condition of continuous high current. With digital graphic processing technique, images were processed in real time by MAQ module of Labview. The best morphological processing approach was obtained by comparing the width of molten pool extracted in various image processing methods. The width of molten pool can be measured and the data can be saved automatically. It laid a foundation for the realization of quality control in double electrode MIG welding.

Key words bypass coupled arc; molten pool edge extraction; morphology tracking and technique of large fillet weld seam of mobile welding robot MAO Zhijue¹, LI Shuyang, GE Wenao, PAN Jijuan, ZHANG Hua (1. Robot and Welding Automation Laboratory, Nanchang University, Nanchang 330029, China; 2. Department of Mechanical Engineering, Tsinghua University, Beijing 100084, China), P 33—36

Abstract For the problem that the uniform welding speed leads to bad shape at the peak of fillet weld seam during tracking the large fillet weld seam of mobile welding robots, the method of welding current adjusted on line and in time according to the welding speed is presented. First, Kinematic analysis of the large fillet weld seam tracking is given, and the welding speed is changed follow cosine law to achieve the normal welding. Then, welding current is adjusted on line according to the changes of welding speed in welding process. Welding current matched to welding speed is gained by experiments. By matching experiment, welding current at the fillet position matched to the aver-